

Intelligent Guidance and Trajectory Command Systems for Autonomous Space Vehicles

John D. Schierman,^{*} David G. Ward,[†] Jason R. Hull,[‡] and Neha Gandhi[§]

BARRON ASSOCIATES, INC.
Charlottesville, VA 22901

Abstract

This effort represents continued developments of an integrated reconfigurable control, adaptive guidance, and onboard trajectory command reshaping system that was successfully flight tested in 2003. The purpose of these advanced algorithms is to recover the mission in the face of severe off-nominal conditions and control effector failures. In the flight test program, the system was developed for the mission's final flight phase known as approach and landing. The current effort is furthering the technology with application to other flight phases such as re-entry and Terminal Area Energy Management (TAEM). The guidance law utilizes a backstepping architecture to generate attitude rate commands that drive the inner-loop control system. Under certain control surface failure conditions, the bandwidth of the inner-loop control system is purposely reduced to lessen the commanded moments. In these cases, the guidance feedback gains are adapted on-line to preserve stability margins in the guidance loops in the face of degraded maneuvering capabilities. During the course of the flight test program, it was shown that failure scenarios that significantly alter the energy management of the vehicle will require the commanded trajectory to be reshaped in order to achieve an acceptable touchdown - even with reconfigurable/adaptive control and guidance. The onboard trajectory reshaping algorithm is known as the Optimum-Path-To-Go (OPTG) approach. OPTG results from the flight test program will be reviewed. However, new results of trajectory command reshaping during the TAEM guidance flight phase will also be presented. In this flight phase, the altitude and velocity must be brought to acceptable values at the start of the final approach. Further, the Heading Alignment Cone, or HAC turn, is flown to align the vehicle's heading with the runway centerline. It will be shown that the OPTG algorithm can successfully reshape the HAC turn due to significant changes in the vehicle's lift and drag. These changes may come about due to a control effector failure or significant head or tail winds. It will be shown that the mission is able to achieve an acceptable TAEM/final approach interface with trajectory reshaping.

I. Introduction

NASA and the Air Force have focused significant attention in recent years on making new launch systems and space transportation architectures safer, more reliable, and less costly. Because of these interests, there is now substantial concentration in control and guidance system reconfiguration technologies. Although the focus of the work presented herein is on *Reusable Launch Vehicles*, or *RLVs* [1], [2], these new reconfiguration technologies have wide applicability to other space platforms such as the emerging lunar and Mars mission exploration vehicles. On-line reconfiguration can give the vehicle the capability to account for unexpected or unforeseen changes to the dynamics, aerodynamics, or control of the vehicle. Such changes may be due to, for example, structural damage to the vehicle, or control effector failures. However, RLVs typically do not possess the actuation redundancy or alternate control effectors seen in commercial or military aircraft, and this makes the reconfiguration task that much more challenging. Because of this, the reconfiguration problem will often involve not only the control of the

^{*} Senior Research Scientist, 1410 Sachem Pl., Ste. 202, Associate Fellow, AIAA.

[†] Senior Research Scientist, 1410 Sachem Pl., Ste. 202, Senior Member, AIAA.

[‡] Research Scientist, 1410 Sachem Pl., Ste. 202.

[§] Research Associate, 1410 Sachem Pl., Ste. 202.

vehicle, but also the guidance and trajectory command functions as well. A unique approach to the RLV on-line reconfiguration/adaptation problem is discussed herein. Along with a reconfigurable control system, this approach involves two main elements:

1. *Guidance gain adaptation*: An adaptive backstepping approach [3] has been developed to deliver commands to the inner-loop control system. Following an effector failure, information regarding inner-loop bandwidth reduction is delivered to algorithms that adapt the feedback gains of the guidance law. Flight path stability is then maintained in the face of degraded maneuvering capabilities.
2. *On-line trajectory command reshaping*: Even with flight path stability maintained, the trajectory commands driving the guidance system may need to be continually reshaped in flight in order to achieve desired end conditions of the mission segment (e.g. on final approach, desired end conditions are characterized by a soft landing, at a certain runway touchdown point, at a certain flight speed). The approach discussed here is denoted as the *Optimum-Path-To-Go (OPTG)* algorithm [4], [5], [6] [7]. Polynomial networks describing the “best” remaining path to the end of the mission segment are interrogated on-line at regular intervals to obtain the optimal trajectory commands, given the current state and “health” of the vehicle.

The algorithms developed in this effort were successfully flight tested under the Integrated Adaptive Guidance & Control (IAG&C) program, funded by the Air Force Research Laboratory (AFRL) [7]. The flight tests were completed by the Flight and Aerospace Research Group, General Dynamics Advanced Information Systems (GDAIS) - formally Veridian – using the Total In-Flight Simulator (TIFS) research aircraft. The TIFS simulated autonomous approach/landings of Boeing’s X-40A test-bed vehicle (shown in Figure 1) under a variety of single and multiple control surface failure experiments. The majority of the flight test results indicated the significant benefits of the control reconfiguration, guidance adaptation, and trajectory-command reshaping, concluding in successful touchdown conditions. Although most touchdowns were simulated at an altitude of 200 feet, the safety pilots of the TIFS vehicle were comfortable enough with the simulated (unpiloted) system to allow some of the experiments to complete actual touchdowns.

For the current efforts, the demonstration platforms have been Orbital Science Corp.’s X-34 and Boeing’s X-37 RLVs. The X-40A is an 80% scale version of the X-37. The control effectors for the X-37 are left and right ruddervators for both pitch (asymmetric deflection) and yaw/roll (symmetric deflection) control, and left and right flaperons for both lift (symmetric deflection) and roll (asymmetric deflection) control. Additionally, the vehicle is equipped with a bodyflap hinged at the aft of the fuselage, similar in configuration to the Space Shuttle’s body flap. Under nominal operations, this surface is used for pitch trim control, but may be used for active pitch control under failures. Lastly, a speedbrake for velocity control is located on the top of the fuselage between the ruddervators, and can be deflected upward to 70 deg., nominally deflected to approximately 20 deg. so that the velocity can be controlled in both directions (reduce deflection to speed up, increase deflection to slow down). Under certain failure scenarios, the speedbrake can be employed to produce some pitching moment.



Figure 1. Boeing’s X-40A RLV in Drop Tests.

Likewise, the control effectors for the X-34 (shown in Figure 2) are left and right elevons for pitch (symmetric deflection) and roll (asymmetric deflection) control, a bodyflap for pitch trim control, a rudder for yaw control, and a clamshell speedbrake on the leading edge of the vertical tail for velocity control.

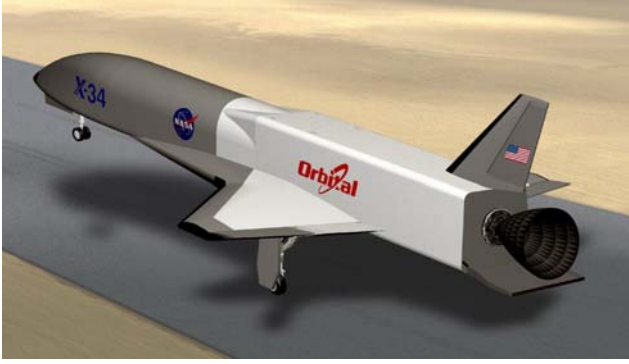


Figure 2. Orbital Science Corporation’s X-34 RLV.

In the flight test program, a detailed design of the adaptive guidance system and on-line trajectory command-reshaping algorithm was integrated with a reconfigurable control system designed by AFRL [8]. The adaptive guidance system, the OPTG trajectory command-reshaping algorithm, and the reconfigurable control system have been presented in detail in [4] through [9]. The adaptive guidance system and the OPTG trajectory reshaping algorithm will be summarized here. Along with a review of flight test results, new results for the TAEM studies will then be presented that show the benefits of trajectory command reshaping.

II. Design Overview

An overview of the design architecture is given in Figure 3. The adaptive backstepping guidance law delivers a pitch rate command to the inner-loop control law. Boeing’s lateral guidance law was adopted to deliver yaw rate and roll rate commands. The lateral guidance law involved classical proportional-integral-derivative (PID) feedback loops on crossrange error, and additional compensation to achieve coordinated flight through turns (i.e. zero sideslip). As indicated in the figure, both measurements and *critical parameters* are supplied to the OPTG trajectory reshaping algorithm and the adaptive guidance laws. Following an anomalous event such as a control effector failure, critical parameters are those measurable

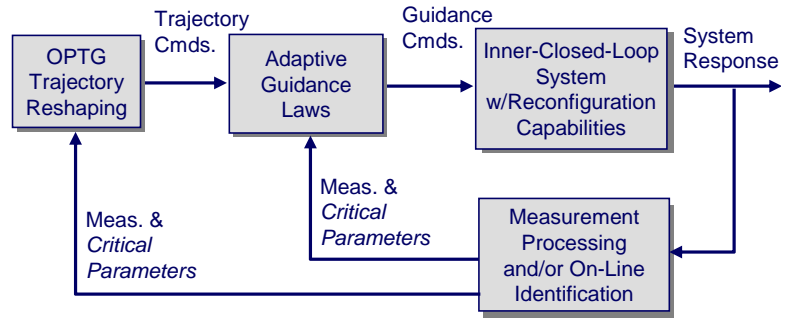


Figure 3. Overview of Design Architecture.

(or reconstructable) quantities that convey the key aspects of the vehicle’s performance degradations to the outer-loop guidance reconfiguration or trajectory reshaping functions. For the current study, the critical parameter for guidance law adaptation is the inner-loop controller’s reference model bandwidth (a design parameter) which is used to schedule outer-loop guidance gains. The critical parameters for trajectory reshaping are upper and lower bounds on achievable lift and drag forces, identified on-line. Analogous to the “attainable moment set,” often discussed in inner-loop attitude control studies, the lift and drag bounds characterize the “attainable force set” – important for the outer-loop guidance problem. Lift and drag bounds parameterize all possible failures and anomalous conditions that affect the vehicle’s ability to generate these forces. For example, the commanded trajectory may be reshaped in the same fashion for an unforeseen headwind as it would for a particular locked control surface that would add approximately the same amount of additional axial force. The lift and drag bound estimates are fed to the OPTG trajectory-reshaping algorithm to determine the appropriate trajectory to follow. The OPTG algorithm then delivers altitude and flight path angle commands to the longitudinal guidance law.

III. X-40A Adaptive Guidance Law Design.

The guidance law design for the IAG&C program is briefly reviewed here. This system consists of three main elements: (1) a backstepping architecture, (2) an adaptive element, coupled with inner-loop reference model bandwidth, and (3) a final flare guidance law. Further details on this design may be found in [9].

A. Backstepping Architecture

For longitudinal guidance, a backstepping approach is employed whereby “pseudo commands” are generated at each loop closure that drives the next-most inner loop [10]. These commands are derived by proportional-plus-integral (PI) control coupled with dynamic inversion. For fixed-wing aircraft systems such as the X-40A, a natural loop-closure architecture that allows for backstepping is:

- i. Altitude loop (outer most loop) to
- ii. Flight-path-angle loop to
- iii. Angle-of-attack loop (inner-most loop).

The last loop then generates the pitch rate command, Q_c , that drives the inner-closed-loop pitch dynamics. This architecture is depicted in Figure 4. Note that the trajectory reshaping algorithm delivers altitude, flight path angle, and flight path angle rate commands ($H_c, \gamma_c, \dot{\gamma}_c$) to the guidance law. These parameters define the commanded trajectory. Also see that the reference model pitch-loop bandwidth, K_{bw_Q} , is fed back to each block for gain adaptation purposes. The guidance laws depicted in each block in Figure 4 will be discussed in more detail below.

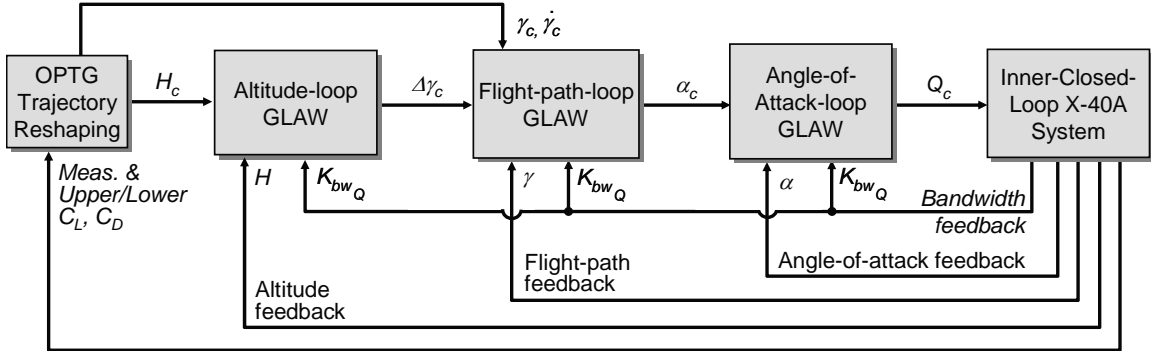


Figure 4. Feedback Architecture.

For the altitude loop guidance law, the governing equation of motion is:

$$\dot{H} = V \sin(\gamma) \quad (1)$$

From dynamic inversion, the flight path command is,

$$\gamma_c = \sin^{-1}(\dot{H}_{des}/V) \quad (2)$$

A corrective flight-path angle command, or $\Delta\gamma_c$, is generated from a corrective sink rate command, $\Delta\dot{H}_{des}$. That is, using Eq. (2), $\Delta\gamma_c$ is defined as,

$$\Delta\gamma_c = \sin^{-1}(\Delta\dot{H}_{des}/V) \triangleq f_\gamma^{-1} \quad (3)$$

Figure 4 indicates that the altitude loop guidance law delivers this corrective value for flight-path angle instead of a total quantity. The corrective sink rate command, $\Delta\dot{H}_{des}$, is derived from PI control on altitude error. In the Laplace domain,** this can be expressed as,

$$\Delta\dot{H}_{des}(s) = \left(K_H + \frac{K_{H_i}}{s} \right) (H_c(s) - H(s)) \quad (4)$$

where the altitude command, $H_c(s)$ is derived from the OPTG algorithm.

Next, the flight-path-angle loop formulates the appropriate angle-of-attack command. The governing equation of motion here is:

$$\dot{\gamma} = \frac{L}{mV} - \frac{g}{V} \cos(\gamma) \quad (5)$$

It is assumed here that total vehicle lift, L , can be expressed as follows:

$$L = L_o + L_\alpha \alpha + \{L_\delta\} \bar{\delta} \quad (6)$$

where L_o is lift at zero angle-of-attack, L_α is the dimensional lift-curve slope, $\{L_\delta\}$ is a row vector of lift increment due to each control surface deflection, and $\bar{\delta}$ is the vector of control surface deflection values.

From dynamic inversion, the angle-of-attack command is,

$$\alpha_c = \frac{mV}{L_\alpha} \left(\dot{\gamma}_{des} + \frac{g}{V} \cos(\gamma) - \frac{L'}{mV} \right) \triangleq f_\alpha^{-1} \quad (7)$$

where, L' is defined as,

$$L' = L_o + \{L_\delta\} \bar{\delta} \quad (8)$$

PI control is again used to derive the desired flight path angle dynamics. Therefore, the desired flight path angle rate is defined in the Laplace domain as:

$$\dot{\gamma}_{des}(s) = \dot{\gamma}_c(s) + \left(K_\gamma + \frac{K_{\gamma_i}}{s} \right) (\gamma_c(s) + \Delta\gamma_c(s) - \gamma(s)) \quad (9)$$

where the flight path angle and flight path angle rate commands, $\gamma_c(s)$, $\dot{\gamma}_c(s)$, are derived from the OPTG algorithm. Again, the corrective term on the flight path angle command, $\Delta\gamma_c(s)$, is derived from the altitude loop guidance law (see Eq. (3)).

The angle-of-attack loop formulates the appropriate pitch rate command for the inner-loop control law. From $\theta = \alpha + \gamma$, and ignoring lateral-directional influences on the pitch rate so that $Q = \dot{\theta}$, the governing equation of motion here is:

$$\dot{\alpha} = -\dot{\gamma} + Q \quad (10)$$

Substituting Eq. (5) for $\dot{\gamma}$, dynamic inversion gives,

** PI control is presented here in the familiar Laplace domain (i.e. for continuous systems) for clarity. Note, however, the actual implementation of the all the algorithms was in the discrete-time domain.

$$Q_c = \dot{\alpha}_{des} - \frac{g}{V} \cos(\gamma) + \frac{L'}{mV} + \frac{L_\alpha}{mV} \alpha \triangleq f_Q^{-1} \quad (11)$$

First order angle-of-attack tracking is desired; hence, the desired angle-of-attack dynamics are defined as:

$$\dot{\alpha}_{des} = K_\alpha (\alpha_c - \alpha) \quad (12)$$

where α_c is the angle-of-attack command generated from the flight-path loop guidance law (Eq. (7)).

From the above equations, the backstepping guidance law is depicted in detail in Figure 5. In the figure, the functions f_γ^{-1} , f_α^{-1} , and f_Q^{-1} are defined in Eqs. (3), (7) and (11), respectively.

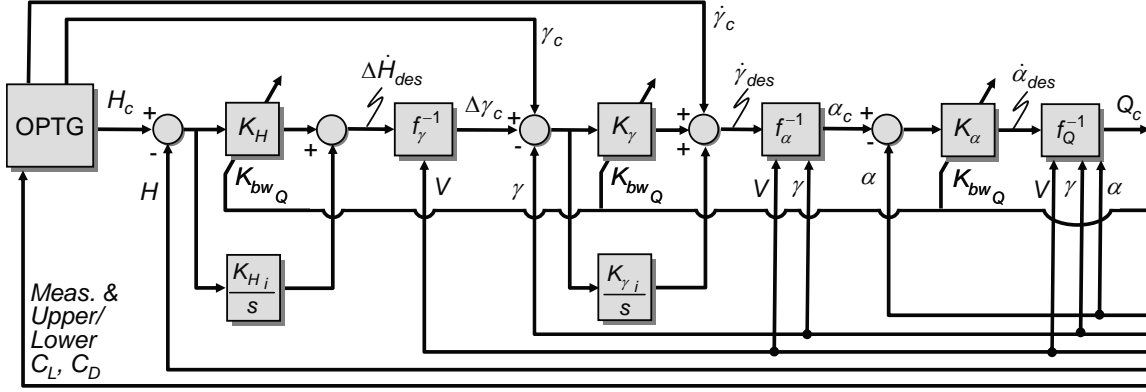


Figure 5. Backstepping Guidance Law in Detail.

B. Guidance Law Gain Adaptation

As shown in Figure 5, the proportional gains within each block of the guidance law are adapted based on the control system's reference model pitch-loop bandwidth, K_{bw_Q} . This reference model design parameter is reduced in the control system when the inner-loop pitch axis becomes saturated. The proportional gains in the guidance law are designed to be linear functions of the pitch axis bandwidth, and this relationship was designed via "loop shaping" considerations. In this manner, when the pitch axis bandwidth is reduced, the proportional gains in each of the guidance loops are reduced to maintain stability robustness margins. The adaptation laws used for the flight test program are given in Table 1. It should be noted that non-adaptive systems often contain logic to address control saturation. The approach here is deemed "adaptive" because the feedback gains adapt to changes in the inner-loop bandwidth. Although here, such changes are due to saturation, the approach can be generalized to address other reasons for bandwidth changes. For example, in some vehicles, not all actuators have equivalent bandwidth capabilities, and if high-bandwidth, primary control effectors fail, slower actuators may have to be utilized in the inner-loop control reconfiguration. In such a case, there will be an overall reduction in inner-loop bandwidth - not due to saturation. The adaptive guidance scheme presented here would be able to address that class of control failures as well.

Table 1. Guidance Loop Gain Adaptation Law.

Loop	Adaptation Law	Nominal Gain Value
Altitude Loop	$K_H = (\frac{1}{15})K_{bw_Q}$	0.2
Flight Path Loop	$K_\gamma = (\frac{1}{5})K_{bw_Q}$	0.6
Angle-of-attack Loop	$K_\alpha = (\frac{5}{9})K_{bw_Q}$	1.67

For the integrator gains, anti-windup logic is added to help preserve stability if saturation occurs in either the angle-of-attack loop or the pitch axis loop of the inner-loop control system. If, for example, the angle-of-attack command exceeds valid bounds defined by the aerodynamic database ($-5 \leq \alpha \leq 24$ deg.), then the integrator states will quickly grow due to tracking errors. A similar situation will occur if the inner loop saturates and can no longer achieve the pitch rate command. For either of these situations, the integrator states in the altitude and flight-path loops are held at their current values.

C. Final Flare Guidance Law

Near touchdown, the primary objective is to arrest the sink rate in preparation for landing. This is accomplished in the final flare guidance law. At an altitude of $H_{ff} = 150$ ft., the guidance law tracks an exponential sink rate profile instead of tracking the trajectory provided by the OPTG algorithm. This profile is generated using a linear relationship between altitude and sink rate, as shown in Figure 6. That is,

$$\dot{H}_c = -\frac{H}{\tau_{ff}} + \dot{H}_{des} \quad (13)$$

Here, $\dot{H}_{des} = -2$ fps is the desired touchdown sink rate.

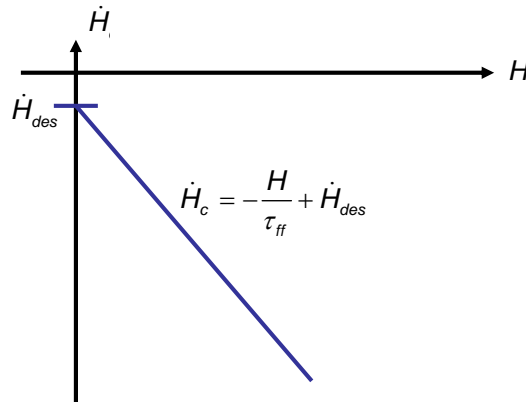


Figure 6. Altitude vs- Sink Rate Profile During Final Flare Guidance.

The time constant is chosen automatically at the start of the final flare to preserve continuity in the sink rate profile. That is,

$$\tau_{ff} = H_{ff} / (\dot{H}_{des} - \dot{H}_{@H_{ff}}) \quad (14)$$

In addition to preserving continuity, this scheme selects a more or less aggressive time constant depending on the magnitude of the sink rate at H_{ff} .

The sink rate command is then converted into a flight path angle command using the relationship given in Eq. (2). The flight path angle rate command is derived by numerically differentiating the flight path angle command.

The final flare guidance scheme was found to be robust to disturbances and other variations, consistently achieving touchdown sink rates well within the acceptable limits.

IV. X-40A Trajectory Command Reshaping Summary

The OPTG trajectory-reshaping algorithm is tasked to find a re-targeted trajectory that requires only forces and moments that can be achieved by the degraded capabilities of the vehicle while meeting certain critical constraints. As shown in Figure 4, the re-targeted trajectory is expressed in terms of altitude, flight path angle and flight path angle rate commands. These commands, derived from the on-line OPTG algorithm, drive the guidance loops. The main steps to the OPTG design protocol are listed below.

A. OPTG Protocol

1. Off-Line Trajectory Optimization Formulation: For the mission segment under study, a trajectory optimization problem is first formulated by defining the objective function, boundaries of admissible initial/final conditions, admissible variations in critical parameters (again, bounds on trim lift and drag), any particular constraints and the appropriate governing equations of motion. Once properly formulated, candidate trajectories can be readily obtained.
2. Off-Line Trajectory Database Generation: A database of neighboring extremals is generated by successively varying initial conditions and critical parameters. Such trajectories represent optimal flight paths for the vehicle under failure conditions. Libraries of trajectory databases are generated by repeating this procedure for several downrange locations (usually in equally spaced intervals). This large volume of trajectory data can be cumbersome to interrogate on-line with traditional table lookup methods. The next step in the OPTG approach solves this problem.
3. Off-Line Trajectory Encoding: This aspect of the OPTG methodology is the most important in terms of enabling on-line use. First, from the set of neighboring extremals found in Step 2, the states of the system are modeled as a set of selected basis functions most appropriate for the mission segment. Polynomials in downrange have been selected for the approach-to-landing flight phase, which is largely 2-dimensional flight (vertical plane motion). A nonlinear function-modeling tool is then used to generate polynomial neural networks (PNNs) that map the current vehicle observables (states and critical parameters) to the coefficients of the basis functions describing the associated trajectory. These mappings relate the observables to the basis function coefficients in an efficient, compact manner.
4. On-Line PNN Interrogation: The final step in the OPTG approach is performed on-line. During flight, the current vehicle states and critical parameters are obtained from measurements or reconstructed from an on-line identification algorithm. This information is then used to compute an appropriate set of basis function coefficients by interrogating the PNNs. Sensor noise and atmospheric disturbances, such as gusts or unpredicted winds, are difficult to include in a trajectory database and thus would not be represented in the PNN models. To be robust to such disturbances and errors, the PNNs are augmented with an on-line coefficient correction algorithm to ensure that the final conditions are met (here, a simple least-squares fit routine has been seen to work quite well). The trajectory commands are then calculated from the corrected basis functions. The loop is closed by re-interrogating the PNNs at regular intervals – typically on the order of 1 Hz. In this manner, trajectories are reshaped in flight to account for changes in the vehicle dynamics due to control surface failures or other significant anomalous events.^{††}

A review of the trajectory optimization formulation for the approach/landing flight phase is given below.

^{††} Note that for the flight test program, only one database of trajectories was generated and then interrogated. This occurred at the beginning of each run. Due to programmatic limitations, all control failures were modeled to occur at the start of the final approach.

B. Trajectory Optimization Formulation

System states appropriate for the approach/landing flight phase are: $\{V = \text{velocity}; \gamma = \text{flight path angle}; X = \text{downrange}; H = \text{altitude}\}$, with the corresponding governing equations of motion:

$$\begin{aligned}\dot{V} &= \frac{-D}{m} - g \sin(\gamma), \quad D = \bar{q} S C_D(\alpha, M) \\ \dot{\gamma} &= \frac{L}{mV} - \frac{g}{V} \cos(\gamma), \quad L = \bar{q} S C_L(\alpha, M) \\ \dot{X} &= V \cos(\gamma) \\ \dot{H} &= V \sin(\gamma)\end{aligned}\tag{15}$$

Here, $D = \text{Drag}$, $L = \text{Lift}$, $g = \text{acceleration of gravity}$, $m = \text{vehicle mass}$, $\bar{q} = \text{dynamic pressure}$, $S = \text{wing area}$, C_D and C_L are the drag and lift coefficients, respectively, $\alpha = \text{angle-of-attack}$, and $M = \text{Mach no.}$ To attain additional robustness, common practice in RLV trajectory optimization is to change the independent variable from time to a monotonic parameter. An appropriate choice for approach/landing guidance is downrange position, X . To do this, each state equation is multiplied by

$$\frac{dt}{dX} = \frac{1}{V \cos(\gamma)}\tag{16}$$

resulting in:

$$\begin{aligned}\frac{dV}{dX} &= \dot{V} \frac{dt}{dX} = V_x = \frac{-D}{mV \cos(\gamma)} - \frac{g}{V} \tan(\gamma) \\ \frac{d\gamma}{dX} &= \dot{\gamma} \frac{dt}{dX} = \gamma_x = \frac{L}{mV^2 \cos(\gamma)} - \frac{g}{V^2} \\ \frac{dH}{dX} &= \dot{H} \frac{dt}{dX} = H_x = \tan(\gamma)\end{aligned}\tag{17}$$

Eq. (16) can be eliminated from consideration since the governing equations are time-invariant and there are no boundary conditions on time (it is not of concern how long it takes for the RLV to arrive at touchdown). Hence, an added benefit of the new parameterization is that it reduces the dimensionality of the search domain in the optimization problem.

The optimization problem is formulated as a Successive Quadratic Programming (SQP) [11] problem. For the SQP method, the states and command or decision variables are partitioned into N discrete points. It was found that $N = 100$ is an appropriate choice for approach/landing trajectories. At each point, an approximation is made that generates a solvable quadratic programming *sub-problem* whose solution is used to form the search direction.

The optimization problem is formalized as follows:

$$\min_{\substack{C_L \in \mathbb{R}^N \\ X_f \in \mathbb{R}}} J = (\dot{H}^T W \ddot{H})^{1/2}, \quad \ddot{H} = f(C_L, X_f)\tag{18}$$

The objective of the cost function is to minimize vertical acceleration, \ddot{H} , which is related to the vehicle's normal acceleration, N_z . This allows for smoother, less aggressive trajectories, especially beneficial under control failure scenarios. The weighting matrix, W , is defined as:

$$W = \text{diag}[1 \quad 1 + \frac{1}{N-1} \quad 1 + \frac{2}{N-1} \cdots \quad 2]\tag{19}$$

This weighting scheme emphasizes minimizing accelerations at the end of the trajectory, resulting in less aggressive flares.

The downrange touchdown position, X_f , has an overriding influence on the shape of the trajectories. Therefore, this is included as a decision variable. As expected, for low-energy scenarios, the optimal touchdown point is often near the beginning of the runway, and for high-energy scenarios, it is typically farther down the runway. The other decision variable is the lift coefficient history, defined as

$$C_L = [C_{L_1}, C_{L_2}, \dots, C_{L_k}, \dots, C_{L_N}]^T \quad (20)$$

Both the lift and drag coefficients are constrained to be within their respective upper and lower bounds, as

$$\begin{aligned} C_{L_{\min}} &\leq C_{L_i} \leq C_{L_{\max}}, \quad i = 1, \dots, N \\ C_{D_{\min}} &\leq C_{D_i} \leq C_{D_{\max}}, \quad i = 1, \dots, N \end{aligned} \quad (21)$$

The lift coefficient is considered the single forcing input to the governing equations of motion, as it is assumed that the drag is a linear function of lift. That is, it is modeled that

$$C_{D_i} = \left(\frac{C_{D_{\max}} - C_{D_{\min}}}{C_{L_{\max}} - C_{L_{\min}}} \right) C_{L_i} + \frac{C_{D_{\min}} C_{L_{\max}} - C_{D_{\max}} C_{L_{\min}}}{C_{L_{\max}} - C_{L_{\min}}}, \quad i = 1, \dots, N \quad (22)$$

Typically, drag is more of a parabolic function of lift; however, at this stage it is convenient to describe the lift and drag characteristics by two points, their maximum and minimum (i.e. $\{C_{L_{\min}}, C_{D_{\min}}\}$, $\{C_{L_{\max}}, C_{D_{\max}}\}$). Further, this linear approximation was not found to be limiting because the lift and drag coefficients are determined from a trimmed solution, which is not unique.^{‡‡} That is, in reality, the lift-drag relationship is characterized by a range of parabolas, and the linear relationship used here lies within this range.

Lastly, the optimization is subject to the following terminal constraints:

$$\begin{aligned} X_{f_{\min}} &\leq X_f \leq X_{f_{\max}} \\ V_f &\leq V_{f_{\max}} \\ \dot{H}_f &\geq \dot{H}_{f_{\min}} \\ H_f &= H_{Rnwy} \end{aligned} \quad (23)$$

The downrange touchdown position is constrained to be between the end of the runway and the point at which the minimum distance required to stop is reached (with margin included). This is defined to be: $0 \text{ ft} \leq X \leq 10,000 \text{ ft}$. (this large range is appropriate for the vehicle under study, as RLVs will typically be targeted to exceptionally long runways or dry lake beds for risk mitigation). For the final velocity, $V_{f_{\max}} = 300 \text{ fps}$. Much beyond this value and tire blowout can occur. For touchdown sink rate, $\dot{H}_{f_{\min}} = -10 \text{ fps}$. Damage to the vehicle can occur for sink rates harder than this limit. Lastly, the final altitude is set to the runway altitude, H_{Rnwy} .

Note that, within the SQP algorithm, the terminal values are found by numerically integrating the system in Eq. (17) from an initial downrange, X_o , to the final touchdown point, X_f , driven by the N decision variables in the ‘‘command vector’’ C_L . In this manner, the state equations are implicitly satisfied even though they are not directly defined as constraints.

^{‡‡} The particular trimmed solution used here minimized control surface deflections from zero deg. deflection for all surfaces except speedbrake, which was nominally deflected to 20 deg.

V. Flight Test Results

Flight of the X-40A during approach/landing was studied under both nominal conditions (all control surfaces working) and for a significant number of *locked* control surface failure cases. Due to programmatic constraints, the focus of failure experiments was limited to locked surfaces, as this was deemed one of the more probable types of failures. Other classes of failures, such as floating, missing, damaged, or partially working surfaces would have to be investigated in further developments of this approach. The IAG&C flight test program took place over the course of several months in 2003. The GDAIS facilities are located at the Buffalo-Niagara International Airport, and the actual flight tests were conducted at the nearby Niagara Falls Airport. This airport possesses an approximately 10,000 foot runway, ideal for such testing.

For the final phase of flight tests, typically one or two nominal runs were first completed for each flight for calibration purposes. In addition to these, there were 40 completed evaluation runs testing 21 different failure combinations. The failure combinations were chosen for their extreme trajectory reshaping characteristics, determined from prior batch simulations experiments. Overall, the flight tests were quite successful, and under calm winds, several runs indicated consistent results with the batch simulation experiments, validating the IAG&C designs. Successful results were based on the criteria described in Table 2.

Table 2. Touchdown Specifications.

<i>Touchdown Specification</i>	<i>Failure to meet specs.</i>
Sink rate ≥ -10 fps.	Landing gear or structural damage
Pitch angle ≤ 15 deg.	Tail scrape
Groundspeed ≤ 310 fps.	Tire blowout
Downrange $\leq 10,000$ ft.	Wheel stop off runway

A. Example Flight Test Results

Results for one set of flight test experiments are presented below. This set of experiments was particularly important as it was one of only two experiments where the failure was flown both with and without trajectory reshaping enabled. Further, this failure required the most substantial amount of reshaping in order to recover (changes from the nominal commanded trajectory). The failure was:

Left flaperon failed at -16 deg. (trailing edge up)
Speedbrake failed at +55 deg. (up)

The failure occurs at approximately 3 nautical miles down range from the runway. Figure 7 presents the trajectory profile (altitude -vs- downrange). Plotted are the reshaped commanded trajectory in the blue solid line (obtained from the OPTG algorithm during flight), the trajectory for the vehicle that follows the reshaped commands in the green dashed line, and the trajectory for the vehicle with no on-line trajectory reshaping in the red dashed line. Note that for both cases, with and without trajectory reshaping, the inner-loop control reconfiguration and guidance loop adaptation are active. For the case with no reshaping, the vehicle cannot follow the nominal trajectory through the main flare, and subsequently hits the ground hard. Obviously for safety reasons, this experiment was performed with the simulated altitude runway defined at 200 ft above the ground. For the case with trajectory reshaping, the OPTG algorithm correctly assigns a commanded trajectory that will not violate the new lift and drag characteristics of the failed vehicle. This results in a trajectory whereby the main objective is to preserve the vehicle's energy, given the substantial increase in drag due to both the flaperon and the speedbrake stuck at such a large deflections. It can be seen that the vehicle first dives at a glideslope steeper than nominal. This is done so that it has enough energy to then level off and fly a horizontal path for approximately 0.5 nautical miles. This extends the vehicle's range so that a legitimate touchdown point can be reached in the face of the increased drag. The second steep glideslope allows the vehicle to maintain enough velocity so that a smooth main flare can be executed (the higher the velocity, the more effective the remaining aerodynamic control surfaces become).

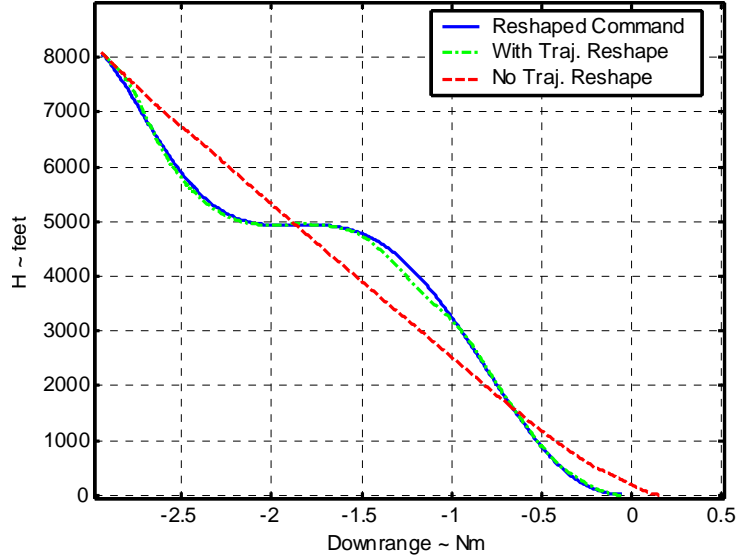


Figure 7. Flight Test Results: Trajectory Profile – Altitude –vs- Downrange.

For the case with no trajectory reshaping, the touchdown sink rate is approximately -17 fps. This hard touchdown occurs because the vehicle does not have enough energy left to perform a proper main flare before touchdown (i.e. at the point where the pull-up is needed for a soft landing, the vehicle's velocity is too low for the control surfaces to have the control power required to execute the pull-up). If not destroying the vehicle outright, this would undoubtedly cause major structural damage. However, the touchdown sink rate for the case with trajectory reshaping is approximately -9.8 fps, within the acceptable limits of the X-40A.

VI. TAEM Trajectory Reshaping for the X-34

As an initial study of the trajectory reshaping problem for the Terminal Area Energy Management (TAEM) flight phase, the X-34 RLV was used as the demonstration platform. The appropriate governing equations of motion for the vehicle during TAEM are:

$$\begin{aligned}
 \dot{V} &= \frac{-D}{m} - g \sin(\gamma) \\
 \dot{\gamma} &= \frac{L \cos(\mu)}{mV} - \frac{g}{V} \cos(\gamma) \\
 \dot{\chi} &= \frac{L \sin(\mu)}{mV \cos(\gamma)} \\
 \dot{X} &= V \cos(\gamma) \cos(\chi) \\
 \dot{Y} &= V \cos(\gamma) \sin(\chi) \\
 \dot{H} &= V \sin(\gamma)
 \end{aligned} \tag{24}$$

Where: $\{V = \text{velocity}; \gamma = \text{flight path angle}; \chi = \text{velocity vector heading angle}; X = \text{downrange}; Y = \text{crossrange}; H = \text{altitude}; \mu = \text{bank angle about the velocity vector}\}$, and:

$$L = \bar{q} S C_L, C_L = C_L(\alpha, M), M = \text{Mach Number}$$

$$D = \bar{q} S C_D, C_D = C_D(\alpha, M)$$

$$\bar{q} = \frac{1}{2} \rho(H) V^2$$

The X-34 vehicle aerodynamics are incorporated through a set of polynomial neural network (PNN) models of the lift and drag coefficients. The inputs to the PNNs are angle-of-attack and Mach no. and the PNNs produce trim $C_L(\alpha(t), M(t))$ and $C_D(\alpha(t), M(t))$.

The optimization problem is posed as follows:

$$\min_{\alpha, \mu \in \mathbb{R}^N} J = k_1 \ddot{H}(\alpha, \mu)^T W_1 \ddot{H}(\alpha, \mu) + k_2 \bar{X}_f(\alpha, \mu)^T W_2 \bar{X}_f(\alpha, \mu) \quad (25)$$

where,

$$\bar{X}_f = [V_f \quad \gamma_f \quad \chi_f \quad X_f \quad Y_f \quad H_f]^T \quad (26)$$

Subject to:

$$\begin{aligned} V_f &= V_o + \int_{t_o}^{t_f} \left(\frac{1}{m} S\bar{q}(t) C_D(\alpha(t), M(t)) - g \sin(\gamma(t)) \right) dt \\ \gamma_f &= \gamma_o + \int_{t_o}^{t_f} \left(\frac{S\bar{q}(t) C_L(\alpha(t), M(t)) \cos(\mu(t))}{mV(t)} - \frac{g}{V(t)} \cos(\gamma(t)) \right) dt \\ \chi_f &= \chi_o + \int_{t_o}^{t_f} \frac{S\bar{q}(t) C_L(\alpha(t), M(t)) \sin(\mu(t))}{mV(t) \cos(\gamma(t))} dt \\ X_f &= X_o + \int_{t_o}^{t_f} V(t) \cos(\gamma(t)) \cos(\chi(t)) dt \\ Y_f &= Y_o + \int_{t_o}^{t_f} V(t) \cos(\gamma(t)) \sin(\chi(t)) dt \\ H_f &= H_o + \int_{t_o}^{t_f} V(t) \sin(\gamma(t)) dt \end{aligned} \quad (27)$$

$$\alpha_{\min} \leq \alpha(t_i) \leq \alpha_{\max}, \quad i = 1, 2, \dots, N, \quad N = \text{no. integration steps}$$

$$\mu_{\min} \leq \mu(t_i) \leq \mu_{\max}, \quad i = 1, 2, \dots, N$$

The objective of minimizing the first term in the cost function given in Eq. (25) is to minimize the vertical acceleration, \ddot{H} , which, again indirectly minimizes the vehicle's normal acceleration. The objective of minimizing the second term in the cost function is to approach desired end conditions at the TAEM-approach/landing interface. Numerical integration of the equations of motion is folded into the constraints that define the end conditions, given in Eq. (27). Lastly, note that angle-of-attack and bank angle are the decision variables, and their optimal histories are sought. The upper and lower bound constraints defined for the angle-of-attack and bank angle are also given in Eq. (27). Reducing these bounds reflects a vehicle under some type of system failure, and leads to reshaped trajectories. Several case studies were performed using this optimization formulation, presented next.

Case 1. HAC Turn Reshaping; Modified Drag

First, we isolated the trajectory to the Heading Alignment Cone, or HAC turn. In this initial case study, the vehicle drag is modified – both increases and decreases in drag are studied here. Again, such cases are representative of a vehicle under a control failure or other vehicle damage that will either increase or decrease vehicle drag – depending on how the inner-loop control system reconfigures the remaining working control effectors, and how the vehicle is re-trimmed. Five runs are shown in the figures below – (1) nominal drag, (2) 20% increase in drag, (3) 50% increase in drag, (4) 20% decrease in drag, and (5) 40% decrease in drag. For these cases, Figure 8 plots their

altitude histories and Figure 9 plots the HAC turn groundtracks. No limitations on lateral maneuvering capabilities are considered at this point. Because of this, the majority of reshaping can be seen to be in the horizontal plane. Although some reshaping is noted in the altitude histories, the more significant reshaping can be seen in the groundtracks. Here, higher energy conditions (less drag) result in wider HAC turns – longer groundtracks to dissipate energy, and lower energy conditions (more drag) result in tighter HAC turns – shorter groundtracks to preserve energy.

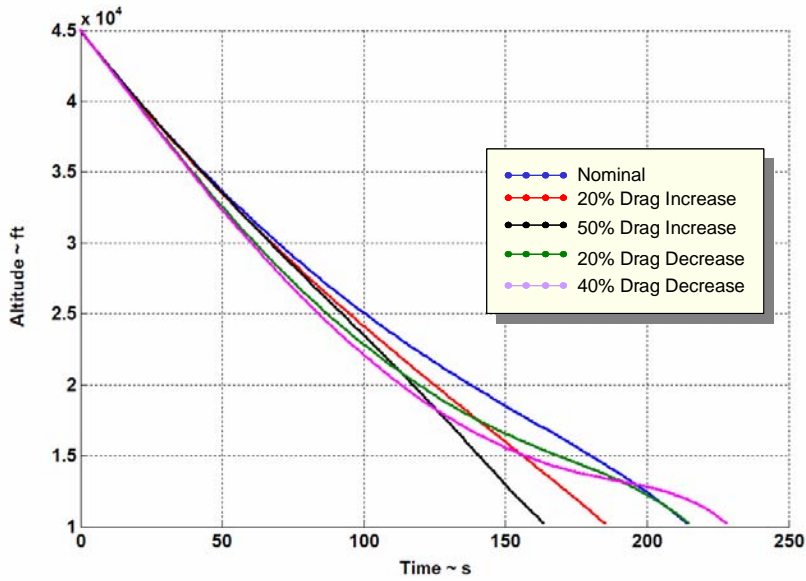


Figure 8. Altitude Histories for Case 1.

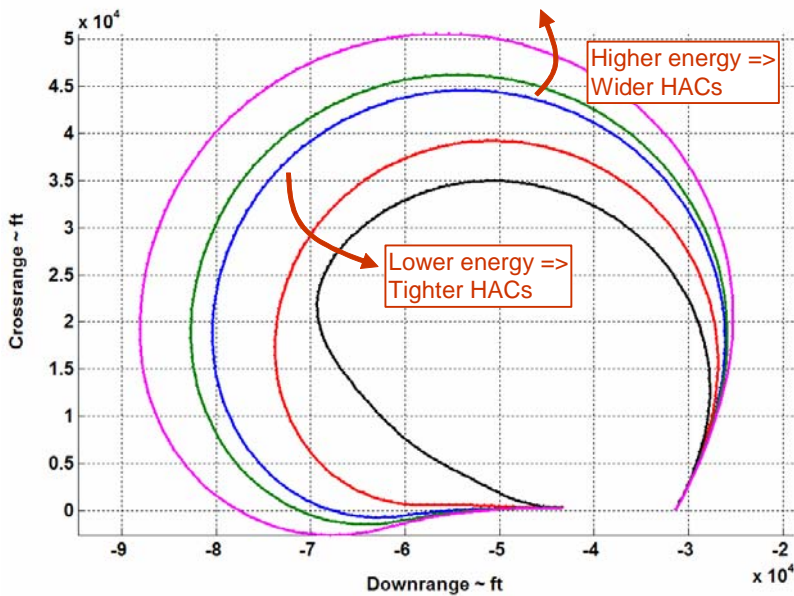


Figure 9. Groundtracks for Case 1.

Case 2. HAC Turn Reshaping; Modified Lift

In this case study, the vehicle lift is modified – both increases and decreases in lift are studied here. Three runs are shown in the figures below – (1) nominal lift, (2) 50% increase in lift, and (3) 50% decrease in lift. For these cases, Figure 10 plots their altitude histories and Figure 11 plots the HAC turn groundtracks. Again, no limitations on lateral maneuvering capabilities are considered at this point. Because of this, the majority of reshaping can be seen to be in the horizontal plane. Although the altitude histories show an increase and decrease in glideslopes from the nominal, there are no dramatic pull-ups or push-overs differing greatly from the nominal case. However, from the groundtrack plots, it can be seen that the higher energy condition (more lift) results in a much wider HAC turn – much longer groundtrack to dissipate energy, and the lower energy condition (less lift) results in a much tighter HAC turn – shorter groundtrack to preserve energy.

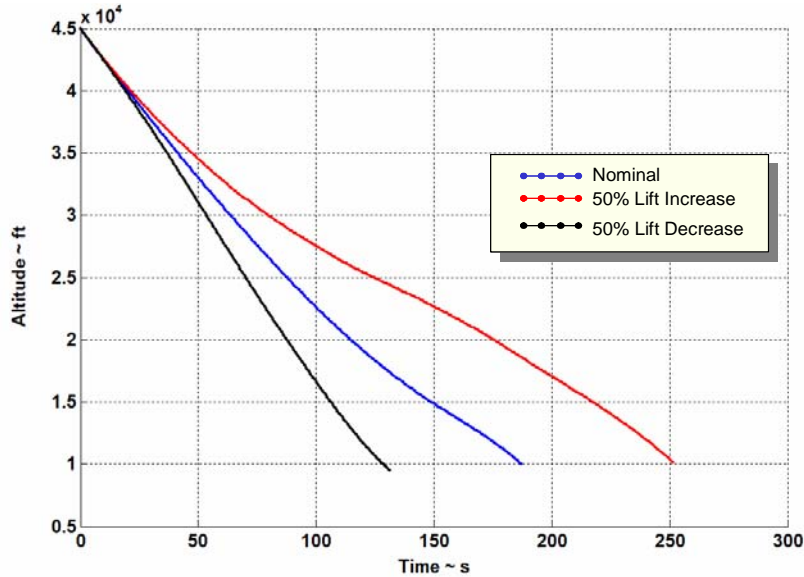


Figure 10. Altitude Histories for Case 2.

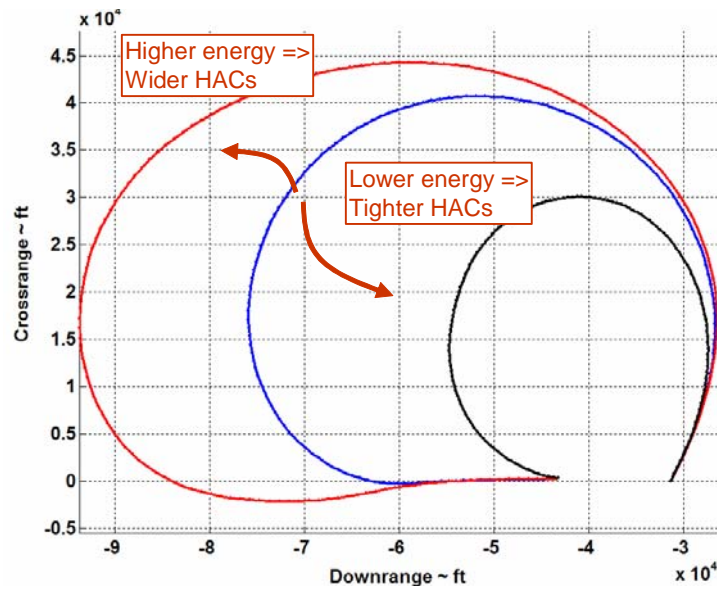


Figure 11. Groundtracks for Case 2.

Case 3. HAC Reshaping; Increased Drag Allowing Higher N_z Maneuvers

In Case 1, the weightings in the cost function (Eq. (25)) were chosen to dominate the vertical acceleration penalty. As such, maneuvers that would result in high normal accelerations, N_z , were not allowed. This case studies the effect of “backing off” on this penalty. Figure 12 shows that reducing this penalty results in a maneuver with a high N_z . For the two cases being compared, drag is increased by 50%. The corresponding groundtrack is much tighter for the case that allows high N_z (as shown in Figure 13). This shows the tradeoff between horizontal and vertical plane reshaping – tighter, more aggressive HAC turns may be beneficial for low energy cases, but can result in vertical plane motion with unacceptably high accelerations. Therefore, the relative cost function weightings are an important design consideration in reshaping TAEM missions.

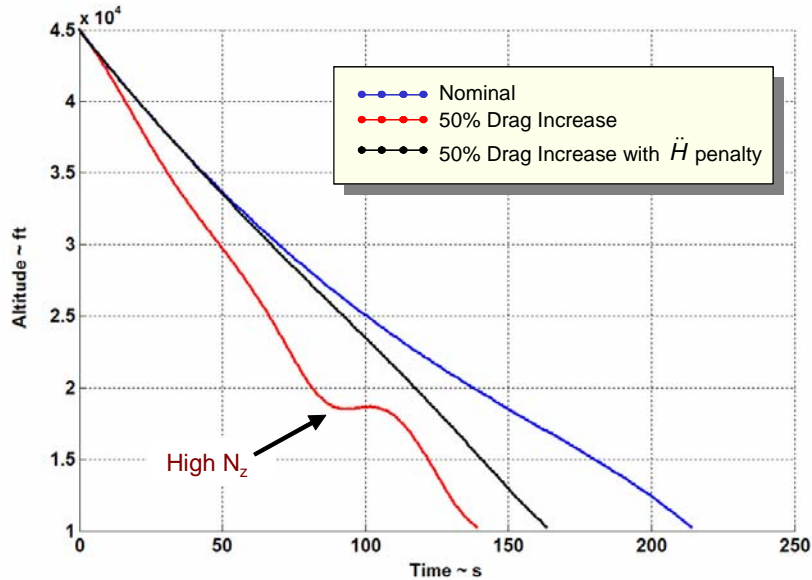


Figure 12. Altitude Histories for Case 3.

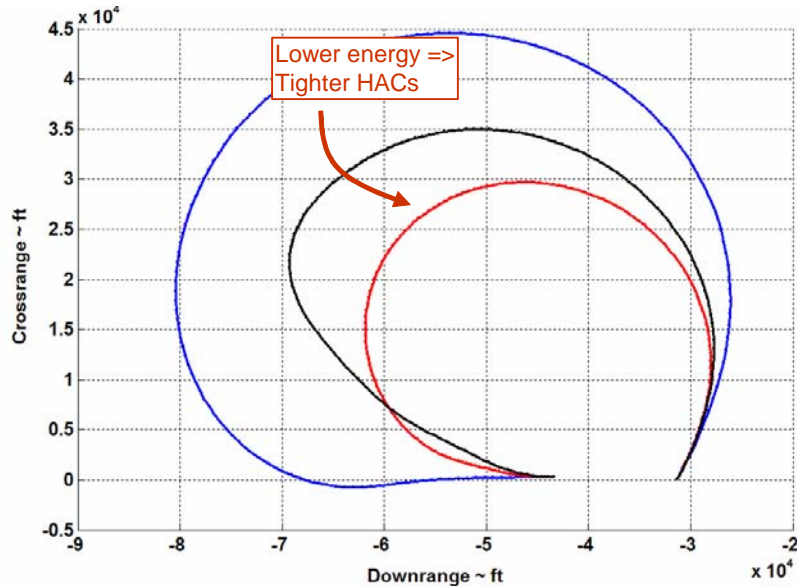


Figure 13. Groundtracks for Case 3.

Case 4. HAC Reshaping; Increased Drag with Bank Angle Limit

Now, limitations on lateral maneuvering capabilities are investigated by limiting the achievable bank angle. Control effector failures, robustness requirements, or limitations on achievable lift may yield such characteristics. Like the previous case, here too, lateral maneuvering limitations result in less aggressive HAC turns. Three runs are shown in the figures below – (1) nominal lift, (2) 50% increase in drag, and (3) 50% increase in drag with the bank angle limited to no greater than 30 deg. For these cases, Figure 14 plots their altitude histories, and Figure 15 plots the HAC turn groundtracks. Figure 14 and Figure 15 show that bank angle limitations cause a combined horizontal *and* vertical plane reshaping solution. That is, as the vehicle has less ability to maneuver laterally, causing a wider HAC turn, the vehicle then pitches up to gain the downrange distance required to fly the longer groundtrack.

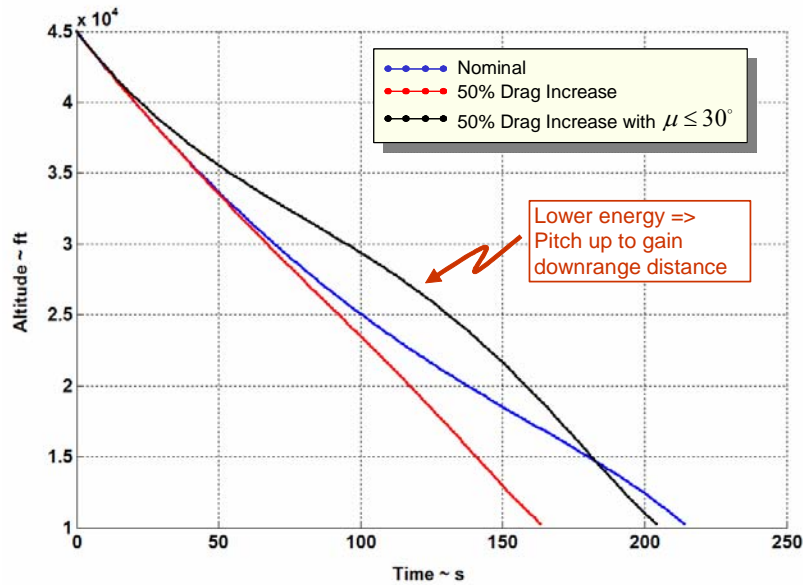


Figure 14. Altitude Histories for Case 4.

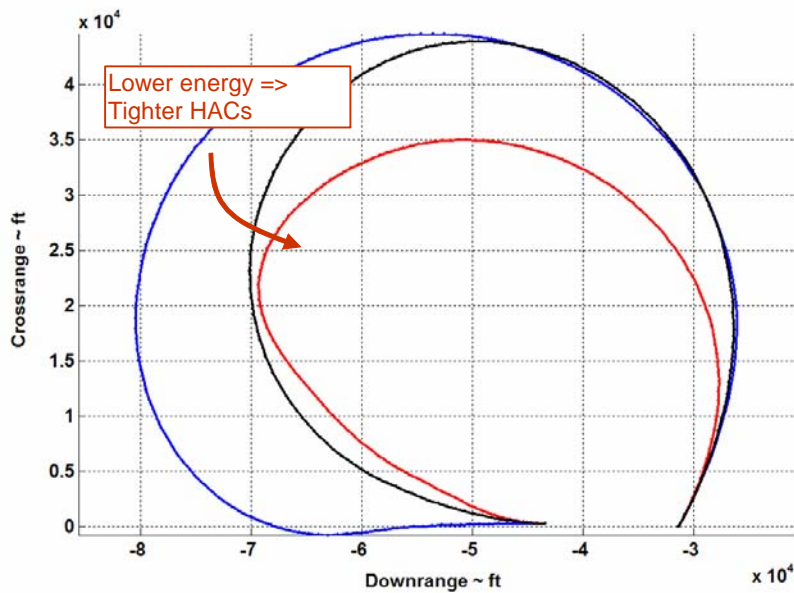


Figure 15. Groundtracks for Case 4.

VII. Preliminary TAEM Trajectory Reshaping Studies for the X-37

The OPTG formulation for TAEM was further matured using an X-37 RLV model supplied by Boeing. Here too, the X-37 vehicle aerodynamics are incorporated through a set of polynomial neural network (PNN) models of the lift and drag coefficients. The inputs to the PNNs are angle-of-attack and Mach no. and the PNNs produce trim $C_L(\alpha(t), M(t))$ and $C_D(\alpha(t), M(t))$.

An improvement to the approach was made by expressing the equations of motion in term of *energy* as the independent variable rather than time. Energy was chosen for the following reasons:

1. it is monotonically decreasing (no singularities in the equations of motion),
2. the desired final energy is fixed since the desired final altitude and velocity are known,
3. formulating the equations of motion in this manner eliminates the final downrange or final time as decision variables, which are not of great importance for this problem, and
4. by defining the final energy state, this eliminates the need for a final velocity constraint (final velocity is determined by final energy and final altitude).

Energy and energy rate are defined as follows,

$$\begin{aligned}
 E &= \frac{1}{2}mV^2 + mgH \\
 \dot{E} &= mV\dot{V} + mg\dot{H} \\
 \dot{E} &= mV\left(-\frac{D}{m} - g \sin(\gamma)\right) + mgV \sin(\gamma) \\
 \dot{E} &= -VD
 \end{aligned} \tag{28}$$

As such, the equations of motion may be expressed as follows,

$$\begin{aligned}
 \frac{\partial V}{\partial E} &= \frac{\partial V}{\partial t} \frac{\partial t}{\partial E} = \frac{1}{mV} + \frac{g}{DV} \sin(\gamma) \\
 \frac{\partial \gamma}{\partial E} &= \frac{\partial \gamma}{\partial t} \frac{\partial t}{\partial E} = \frac{-L \cos(\mu)}{mDV^2} + \frac{g}{DV^2} \cos(\gamma) \\
 \frac{\partial \chi}{\partial E} &= \frac{\partial \chi}{\partial t} \frac{\partial t}{\partial E} = \frac{-L \sin(\mu)}{mDV^2 \cos(\gamma)} \\
 \frac{\partial X}{\partial E} &= \frac{\partial X}{\partial t} \frac{\partial t}{\partial E} = \frac{-1}{D} \cos(\gamma) \cos(\chi) \\
 \frac{\partial Y}{\partial E} &= \frac{\partial Y}{\partial t} \frac{\partial t}{\partial E} = \frac{-1}{D} \cos(\gamma) \sin(\chi) \\
 \frac{\partial H}{\partial E} &= \frac{\partial H}{\partial t} \frac{\partial t}{\partial E} = \frac{-1}{D} \sin(\gamma)
 \end{aligned} \tag{29}$$

A new formulation to the optimization problem is posed as follows:

$$\text{Min}_{\substack{\alpha \in \mathbb{R}^N \\ \mu \in \mathbb{R}^N}} J = k_1 \left(\bar{q} - \bar{q}_{ref} \right)^T \left(\bar{q} - \bar{q}_{ref} \right) + k_2 \ddot{H} \tag{30}$$

Subject to:

$$\begin{aligned}
 & \text{abs} \left(\gamma_f - \gamma(e_o) + \int_{e_o}^{e_f} \left(\frac{-L \cos(\mu)}{mDV^2} + \frac{g}{DV^2} \cos(\gamma) \right) de \right) \leq \gamma_{tol} \\
 & \text{abs} \left(\chi_f - \chi(e_o) + \int_{e_o}^{e_f} \frac{L \sin(\mu)}{mDV^2 \cos(\gamma)} de \right) \leq \chi_{tol} \\
 & \text{abs} \left(X_f - X(e_o) + \int_{e_o}^{e_f} \frac{-1}{D} \cos(\gamma) \cos(\chi) de \right) \leq X_{tol} \\
 & \text{abs} \left(Y_f - Y(e_o) + \int_{e_o}^{e_f} \frac{-1}{D} \cos(\gamma) \sin(\chi) de \right) \leq Y_{tol} \\
 & \text{abs} \left(H_f - H(e_o) + \int_{e_o}^{e_f} \frac{-1}{D} \sin(\gamma) de \right) \leq H_{tol}
 \end{aligned} \tag{31}$$

where $\{\gamma_f \ \chi_f \ X_f \ Y_f \ H_f\}$ are the nominal TAEM/approach & landing interface conditions. One of the main objectives in Boeing's baseline TAEM guidance law is to track a desired dynamic pressure profile. Therefore, the first term in the cost function minimizes variations from the nominal qbar profile. As before, the objective of minimizing vertical acceleration, \ddot{H} , is also included in the cost function. Numerical integration of the equations of motion is folded into the constraints that define tolerances on the TAEM/approach & landing interface conditions. As before, angle-of-attack and bank angle are the decision variables, and their optimal histories are sought.

Several preliminary experiments were performed for this OPTG formulation. Again, the focus here was on the HAC turn portion of the TAEM flight phase. This was done to mimic the actual drop test of the X-37 from a B-52 carrier aircraft. Such flight tests are planned for the near future. The following figures plot the altitude and ground track histories for the nominal (no failures) case. It can be seen that the results are consistent with the Boeing baseline trajectory. Although not shown, all other state histories were also similar to the baseline histories supplied by Boeing.

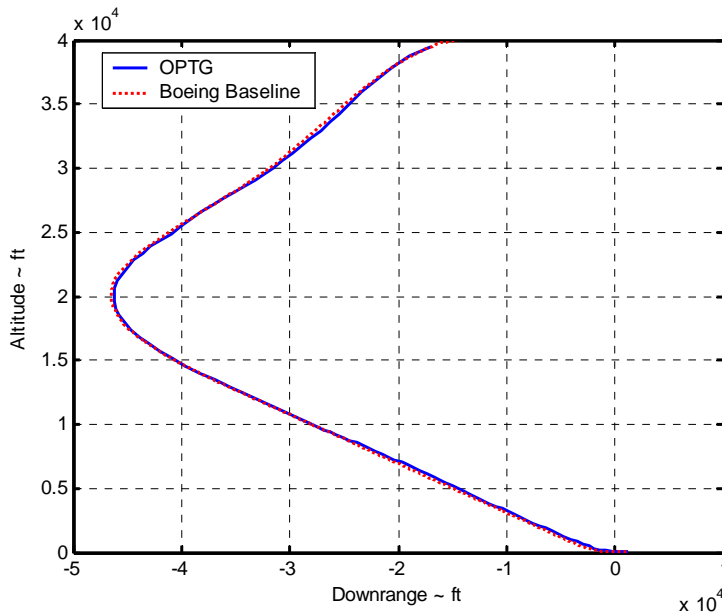


Figure 16. Nominal Altitude Profile for the X-37.

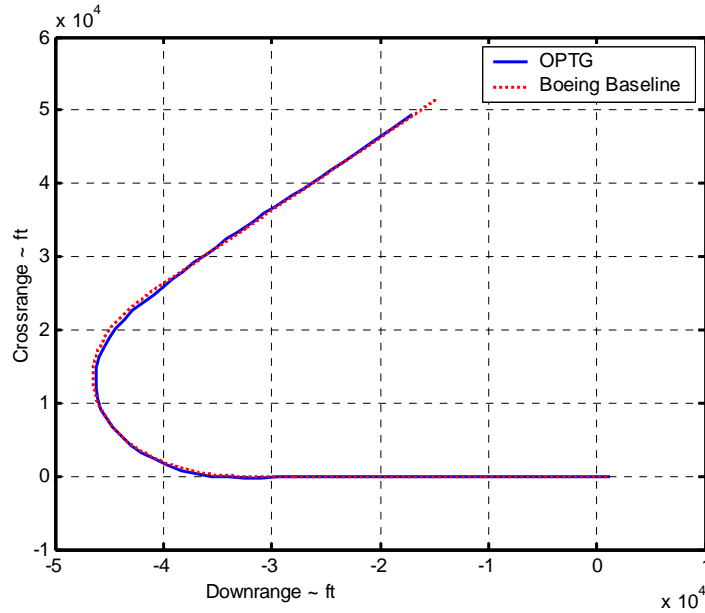


Figure 17. Nominal Ground Track for the X-37.

Next, a low energy failure was investigated. Here, a drag bias was added that was representative of a speedbrake locked at 65 deg. and bodyflap locked at 20 deg. Plotted below are the altitude profile and ground track. As expected, the ground track shows that the vehicle performs a much tighter HAC turn to shorten the range-to-go. The altitude profile shows a pitch up maneuver in the approach & landing flight phase, consistent with past results for low energy cases. (Although not discussed, note that a trajectory optimization problem was formulated for the approach/landing (A/L) flight phase, and the TAEM and A/L trajectory solutions were then “pieced together.”)

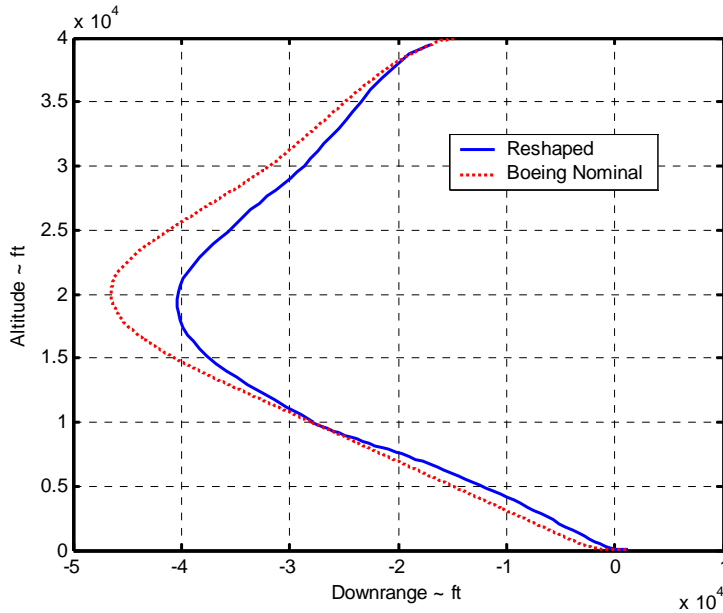


Figure 18. Low Energy Case: Altitude Profile for the X-37.

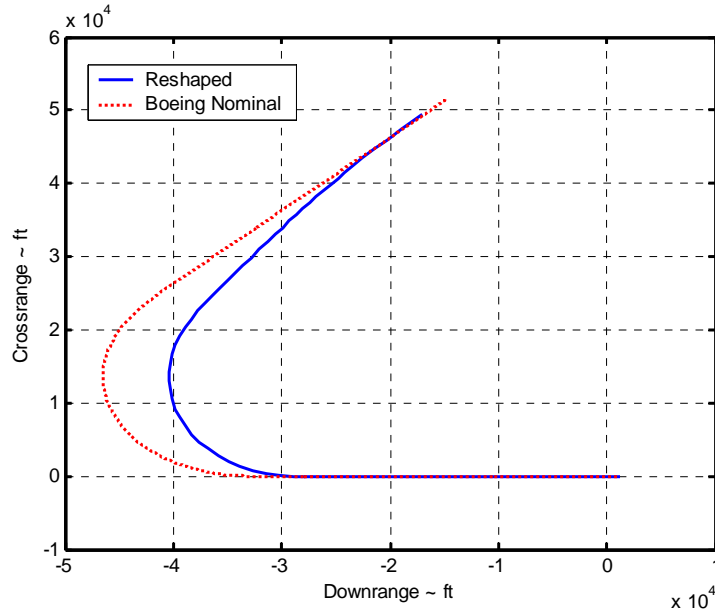


Figure 19. Low Energy Case: Ground Track for the X-37.

Next, a high energy failure was investigated. Here, a drag bias was subtracted that was representative of a speedbrake locked at 0 deg. and bodyflap locked at 0 deg. Plotted below are the altitude profile and ground track. As expected, the ground track shows that the vehicle performs a much wider HAC turn to lengthen the range-to-go in order to dissipate energy.

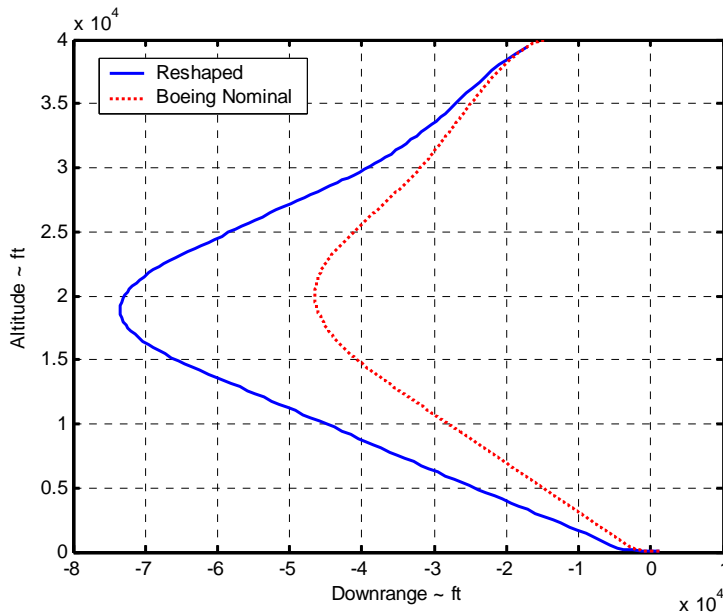


Figure 20. High Energy Case: Altitude Profile for the X-37.

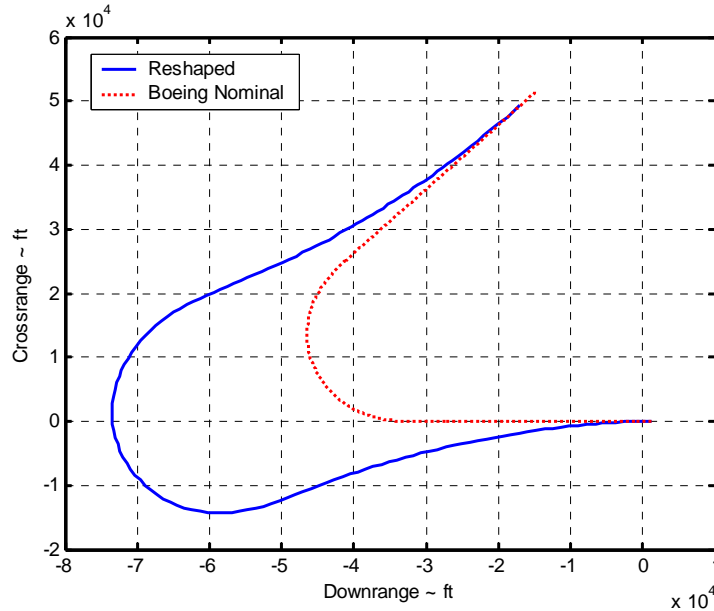


Figure 21. High Energy Case: Ground Track for the X-37.

Note that for this second case, the severity of the failure precluded adhering to the nominal TAEM/approach & landing interface conditions. Although the nominal interface condition could be achieved by the TAEM optimization, the trajectory solution for the approach/landing problem was unrealistic. This approach required large excursions from the nominal glideslope or the runway centerline very near touchdown in order to dissipate enough energy for acceptable end conditions. Instead, the TAEM optimization formulation *was extended to touchdown*, and the approach/landing formulation was not used. In this manner, the maneuvers were more reasonable and the desired end conditions could be met. This case study has indicated that if the failure occurs at higher altitudes, farther from the runway, then there is more design freedom in shaping the trajectory path, and recovery is possible for a wider class of failures. If the failure occurs closer to the runway, trajectory reshaping options become more limited.

As a final note, the wide HAC-turn maneuver seen in Figure 21 may not be desirable as it results in the vehicle flying significantly farther away from the runway. There is always the risk that the vehicle’s energy could change rapidly due to unexpected winds, for example, leaving too little energy to make it to the end of the runway. We are currently investigating using S-turn maneuvers that will “dump” lift as a means to dissipate excess energy without substantial excursions from the runway.

VIII. Conclusions

An adaptive guidance system and an autonomous trajectory command reshaping algorithm were presented. These advanced feedback systems were developed for a class of next generation Reusable Launch Vehicles (RLVs). The guidance law and trajectory reshaping system work in an integrated fashion with a reconfigurable control system to recover the vehicle in the face of severe off-nominal conditions or control effector failures. The guidance law utilizes a backstepping architecture to generate attitude rate commands that drive the inner-loop control system. Under certain control surface failure conditions, the remaining working controls can saturate in an attempt to meet commanded moments. In these cases, the guidance feedback gains are adapted on-line to preserve stability margins in the guidance loops. Control effector failures that significantly alter the energy management of the vehicle will require trajectory command reshaping to recover the mission and achieve acceptable end conditions. The onboard trajectory reshaping algorithm is known as the Optimum-Path-To-Go (OPTG) approach. In this approach, trajectories are pre-computed offline that account for variations in the lift and drag characteristics of the vehicle (i.e. variations in the vehicle’s energy management). Following this step, the trajectories are encoded as polynomial networks, which are then interrogated during flight using current estimates of the lift and drag characteristics. The resulting reshaped trajectory is flown, which accounts for the changed aerodynamic characteristics of the vehicle.

The algorithms were developed for Boeing's X-40A test-bed vehicle and *flight tested* using the Total In-Flight Simulator (TIFS) research aircraft, simulating X-40A vehicle dynamics. An example set of flight test experiments was presented. The results of these flight tests showed that good touchdown conditions were achieved with trajectory reshaping in the face of a very severe multiple control failure. Without trajectory reshaping, the vehicle would suffer substantial damage – even with active control reconfiguration and guidance adaptation.

The flight test experiments were limited to the approach/landing flight phase. Current efforts are furthering the technology with application to other flight phases, such as re-entry and Terminal Area Energy Management (TAEM). Initial trajectory reshaping results were presented for the X-34 and X-37 RLV systems focusing on the Heading Alignment Cone (HAC turn) portion of TAEM. The optimization problem, as formulated, can combine horizontal and vertical plane reshaping depending on the vehicle's ability to maneuver in these axes. With no limitations on lateral maneuvering capabilities, changes in lift and/or drag (high or low energy conditions) can be addressed mainly with trajectory reshaping in the horizontal plane. The HAC turns that result are either wider for high energy conditions, or tighter for low energy conditions. Vertical plane reshaping is minimal except for cases of severe loss in energy. With additional bank angle limitations, the trajectory optimization solution is a combination of both horizontal and vertical plane reshaping.

Acknowledgements

This work was funded under two SBIR programs sponsored by (1) the Air Force Research Laboratory, Dr. David Doman, Technical Monitor, and (2) the Marshall Space Flight Center, Mr. Greg Dukeman and Dr. John Hanson, Technical Monitors. *Their support is gratefully appreciated.* Acknowledgments are also due to General Dynamics Advanced Information Systems (formally Veridian) for their help and advice in the course of the flight test program, and lastly to Boeing, Huntington Beach, for their significant help and advice during both the flight test program and current efforts to advance the technologies.

References

1. Hanson, J. M., "Advanced Guidance and Control Project for Reusable Launch Vehicles," AIAA-2000-3957, Proc. AIAA Guidance, Navigation, and Control Conf., Denver, CO, August, 2000.
2. Hanson, J., "New Guidance for New Launchers," Aerospace America, March, 2003, pp. 36-41.
3. Sharma, M., "Flight-Path Angle Control via Neuro-Adaptive Backstepping," AIAA-2002-4451, Proc. AIAA Guidance, Navigation, and Control Conf., Monterey, CA, Aug. 2002.
4. Schierman, J., Ward, D., Monaco, J., Hull, J., "A Reconfigurable Guidance Approach for Reusable Launch Vehicles," AIAA-2001-4429, Proc. AIAA Guidance, Navigation, and Control Conf., Montreal, Canada, August, 2001.
5. Schierman, J., Hull, J., Ward, D., "Adaptive Guidance with Trajectory Reshaping for Reusable Launch Vehicles," AIAA-2002-4458, Proc. AIAA Guidance, Navigation, and Control Conf., Monterey, CA, Aug. 2002.
6. Schierman, J., Hull, J., Ward, D., "On-Line Trajectory Command Reshaping for Reusable Launch Vehicles," AIAA-2003-5439, Proc. AIAA Guidance, Navigation, and Control Conf., Austin, TX, Aug. 2003.
7. Schierman, J.D., Ward, D.G., Hull, J.R., Gandhi, N., Oppenheimer, M.W., Doman, D.B., "An Approach to Integrated Adaptive Guidance and Control with Flight Test Results," accepted for publication in the *Journal of Guidance, Control, and Dynamics*, approx. 2004.
8. Oppenheimer, M., Doman, D., "Reconfigurable Inner Loop Control of a Space Maneuvering Vehicle," AIAA-2003-5358, Proc. AIAA Guidance, Navigation, and Control Conf., Austin, TX, Aug. 2003.

9. Schierman, J., Gandhi, N., Hull, J., and Ward, D., "Flight Test Results of an Adaptive Guidance System for Reusable Launch Vehicles," AIAA Paper 2004-4771, Proc. AIAA Guidance, Navigation, and Control Conference, Providence, Rhode Island, Aug., 2004.
10. Sharma, M., "Flight-Path Angle Control via Neuro-Adaptive Backstepping," AIAA Paper 2002-4451, August, 2002.
11. Powell, M., "Variable Metric Methods for Constrained Optimization," *Mathematical Programming: The State of the Art*, (A. Bachem, M. Grotchel and B. Korte, eds.) Springer Verlag, 1983, pp. 288-311.